



**HAL**  
open science

## Laser processing of carbon black reinforced ethylene-butyl acrylate copolymer

I. El Aboudi, Z. Bouyahia, Delong He, Jindo Bai, A. Mdarhri, C. Brosseau, A. Benayad, F. Charlot, M. Elazhari, G. Pecastaings

► **To cite this version:**

I. El Aboudi, Z. Bouyahia, Delong He, Jindo Bai, A. Mdarhri, et al.. Laser processing of carbon black reinforced ethylene-butyl acrylate copolymer. *Journal of Applied Polymer Science*, 2023, 140 (40), pp.1-17. 10.1002/app.54486 . hal-04240592v2

**HAL Id: hal-04240592**

**<https://hal.science/hal-04240592v2>**

Submitted on 10 Oct 2024


**HAL** is a multi-disciplinary open access archive for the deposit and dissemination of scientific research documents, whether they are published or not. The documents may come from teaching and research institutions in France or abroad, or from public or private research centers.

L'archive ouverte pluridisciplinaire **HAL**, est destinée au dépôt et à la diffusion de documents scientifiques de niveau recherche, publiés ou non, émanant des établissements d'enseignement et de recherche français ou étrangers, des laboratoires publics ou privés.



Distributed under a Creative Commons Attribution - NonCommercial 4.0 International License

# Laser processing of carbon black reinforced ethylene-butyl acrylate copolymer

I. El Aboudi<sup>1</sup> | Z. Bouyahia<sup>1,2</sup> | D. He<sup>2</sup> | J. Bai<sup>2</sup> | A. Mdarhri<sup>1</sup> |  
C. Brosseau<sup>3</sup>  | A. Benayad<sup>4</sup> | F. Charlot<sup>5</sup> | M. Elazhari<sup>1</sup> | G. Pecastaings<sup>6</sup>

<sup>1</sup>Faculty of Sciences & Techniques, Cadi Ayyad University, Marrakech, BP, Morocco

<sup>2</sup>Laboratoire Mécanique des Sols, Structures et Matériaux (MSSMat), UMR CNRS 8579, CentraleSupélec, Université Paris Saclay, Gif-sur-Yvette, France

<sup>3</sup>Univ Brest, CNRS, Lab-STICC, UMR CNRS 6285, Brest Cedex 3, CS, France

<sup>4</sup>CEA-LITEN, Université Grenoble Alpes, Grenoble Cedex 9, France

<sup>5</sup>Université Grenoble Alpes, CNRS, Grenoble INP, SIMAP, Grenoble, France

<sup>6</sup>Bordeaux INP, Université de Bordeaux, CNRS, LCPO – UMR 5629, Pessac, France

## Correspondence

C. Brosseau, Univ Brest, CNRS, Lab-STICC, UMR CNRS 6285, CS, 93837, 6 avenue Le Gorgeu, 29238, Brest Cedex 3, France.

Email: [brosseau@univ-brest.fr](mailto:brosseau@univ-brest.fr)

## Abstract

Interest in the phenomenon of laser ablation (LA) has gained significant attention in recent years due to its potential for machining, high-precision drilling, and cutting materials, such as metals, semiconductors, and dielectrics. Here, LA of ethylene-butyl acrylate (EBA) filled with different volume fractions (4%, 8%, and 20%) of CB particles is studied. Upon irradiation with the second harmonics (532 nm) of the nanosecond pulsed Nd:YAG laser, a structuration is evidenced at the sample surface in a restricted range of fluence and at high pulse number (PN) (500 pulses, 1 Hz). The laser-ablated surface is analyzed by microtopography, scanning electron microscopy (SEM), and x-ray photoelectron spectroscopy (XPS). Collectively, our data show a lowering in ablation threshold and depth for CB volume fractions larger than the conduction threshold (8%), indicating that visible radiation primarily induces photo-thermal effects. After redeposition of the ablation products at the surface, XPS indicates that high CB content in the EBA matrix induces high oxidation level of the composite surface. Furthermore, our results reveal that LA produces a significant proportion of amorphous carbon. Several parameters which affect heat accumulation and CB particle shielding are discussed. Such parameters include laser fluence and repetition rate, and CB content.

## KEYWORDS

ablation kinetics, carbon black particles, elastomer, laser-induced surface structuration, polymer composites

## 1 | INTRODUCTION

There has been continuous development of polymers filled with CB particles for a diversity of applications including microfluidic channels, medical micro-devices, anti-biofouling, optical waveguides, flexible electronics, and so forth.<sup>1</sup> The demand for micromachining and the creation of precise surface microstructures, such as micro-pits and microscale grooves, with exceptional

precision and versatility, has driven the development of advanced techniques in response to various applications.<sup>2</sup> However, achieving surface micro-structuring (SMS) in these composite materials is challenging due to the significant impact of the polymer's elasticity network on their physical properties, as evidenced in previous studies, see for example References 1,3,4.

For elastomer SMS, mechanical processing is avoided because of viscoelasticity. Micro-casting, chemical wet

This is an open access article under the terms of the [Creative Commons Attribution](https://creativecommons.org/licenses/by/4.0/) License, which permits use, distribution and reproduction in any medium, provided the original work is properly cited.

© 2023 The Authors. *Journal of Applied Polymer Science* published by Wiley Periodicals LLC.

etching, plasma etching, laser surface texturing, and 3D printing are the main available micropatterning methods.<sup>5</sup> There are several advantages and drawbacks to each technique. Micro-casting needs a downstream micro-fabrication technique to produce the mold. Chemical wet etching induces chemical contamination of the materials and suffers from poor repeatability due to effects of temperature and etchant concentration.<sup>5</sup> Even if plasma etching is widely used in polymer surface structuring, it has poor selectivity and produces micropatterns with potential radiation damage.<sup>5</sup> 3D printing can produce complicated 3D components, but the material to be processed must be available in a particle-sized powder form.<sup>5</sup> In contrast, laser microstructuring of materials has been attracting increasing interest<sup>2</sup> because of its better accuracy, repeatability, and rapidity. For polymer SMS, laser processing is often selected in order to enhance tribological properties and lifetime of bearing components/or hydrophobicity.<sup>5-7</sup>

Laser structuring of materials can be either self-produced (laser-induced surface structure [LISS]) in specific conditions of irradiation, or carried out by adjusting laser beam parameters, or by using a laser mask with an appropriate shape. LISS has been studied since the early applications of laser processing of materials. For example, periodic ripples and dot patterns with spacing less than 200 nm have been produced far below the ablation threshold on various highly absorbing polymers using a polarized beam of ArF and KrF excimer lasers.<sup>8</sup> LISS investigations of elastomer composites containing CB particles were pioneering by Niino and coworkers.<sup>9-12</sup> Experiments are done at different laser irradiation parameters (pulse duration and number, fluence, wavelength) using a composite sheet made of methyl acrylate polymer and 30% or 50% of CB content. For composites containing 30% of CB, irradiation in air using excimer lasers produces dome-like microstructures at fluence 90 mJ/cm<sup>2</sup> and microsized cone-like structures at 500 mJ/cm<sup>2</sup>,<sup>10</sup> whereas conical microstructures are obtained with the 532 nm of the Nd:YAG laser.<sup>9,12</sup> Additionally, protuberances were not observed for fs UV laser-treated surfaces, where the irradiation induces only surface roughness.<sup>11</sup>

The physicochemical mechanisms involved in laser ablation (LA) of carbon particle-filled polymers have been investigated.<sup>4,9</sup> Carbon fillers have a higher absorption coefficient at excimer or 532 nm of the Nd:YAG lasers,<sup>9,12</sup> resulting in their heating and subsequent heat transfer to the surrounding cold polymer. Notably, the polymer matrix requires lower temperatures for melting or vaporization compared with the carbon particle fillers.<sup>12</sup> Consequently, this causes the matrix to heat up and leads to the thermal ejection of polymer fragments. Upon laser irradiation at moderate fluences, carbon particles remaining at the surface of composite or debris deposited at the surface stick to the molten polymer surface, act as protective

shields and hinder indirect thermal ablation of the material underlying. With repeated pulses, this effect leads to the formation of conical or dome-like morphologies on the composite surface. When higher fluencies and particle numbers (PN) are involved, the laser irradiation causes both the matrix and filler particles to undergo ablation, resulting in the formation of cavities exhibiting waviness and macro pores.<sup>4,9</sup>

Although many reports have been published in the archival literature dealing with LISS of polymers, little attention has been paid for composite materials. Consequently, there are still many open issues in LA of such materials and their SMS as it was reported for CF filled polymers.<sup>3,4</sup> Since the need for composite repair and SMS is increasing as well, further research of the effect of CB content on LA of polymer composites is of great value. In this work, LA of ethylene-butyl acrylate (EBA) copolymer filled with 4%, 8%, and 20% of CB particles using the 532 nm Nd:YAG laser is studied. The 8% content of CB corresponds to the conduction (percolation) threshold, as evidenced in Reference 13. This study uses state-of-the-art methods (scanning electron microscopy [SEM], microtopography, laser flash analyzer for thermal conductivity measurements, and x-ray photoelectron spectroscopy [XPS]) to convincingly investigate the effect of laser fluence, repetition rate, and CB content on LA and SMS of the composites EBA-CB. By understanding the mechanisms involved in LA, it is possible to (i) improve the quality of the surface structuring by optimizing ablation conditions, or to obtain laser spots having clean and abrupt boundaries without a redeposition of debris across the spot periphery and correspondingly with a greater spatial resolution. We wish to mention that our results suggest that the SMS with high porosity can serve as lubricant pockets, enhancing the tribological properties of polymer composites filled with CB. With these advances, polymers filled with CB and other carbonaceous filler particles (CNT, carbon fiber, graphene) can be further developed and characterized by laser sculpture technique to create novel engineering materials for microelectro-mechanical systems, surfaces with anisotropic functionalities, and polymeric electrodes for flexible optoelectronic devices with improved electrical and optical performances.<sup>14</sup>

## 2 | EXPERIMENTAL

### 2.1 | Materials

The electrical and morphological properties of CB particle filled EBA samples are reported in Reference 13. Three samples (4%, 8%, and 20%) from either side of the percolation threshold (8%) are selected. The average size

of the primary CB particles and aggregates are 30 and 150 nm, respectively. Because the optical properties of acrylate copolymers are similar to those of polymethacrylates (transparent and absorb only UV radiations below 290 nm), we expect that the absorption coefficient of neat EBA is close to that of PMMA, close to  $57 \text{ cm}^{-1}$  at 532 nm.<sup>15</sup> CB aggregates geometry, size, and refractive index are important parameters to determine optical properties. Many experimental and simulation studies based on fractal geometry have shown that the real part of the refractive index is ranging from 1.7 to 1.9. Its imaginary part ranges from 0.4 up to 1.1. The imaginary part of the refractive index  $k = 0.6$  at 532 nm is used for the ablation mechanism discussion.<sup>16</sup> The CB particles absorption coefficient  $\alpha$  at 532 nm, given by  $\alpha = 4\pi k/\lambda$ , is  $1.4 \times 10^5 \text{ cm}^{-1}$ .

## 2.2 | Laser irradiation

The experimental setup for laser irradiation is shown in Figure 1.

The second harmonic emission of pulsed Nd:YAG laser (Excel, Surelite II-10) with wavelength 532 nm and pulse duration 7 ns, is used for irradiation. Processing is carried out in air with repetition rate of 1 Hz. The laser beam is described by a Gaussian spatial profile and has a diameter of about 1.2 mm at the sample surface. The laser energy is measured using an energy meter (GENTEC-EO solo2) with a power detector UP19K-15S-VM-D0 at different Q-switch values. The laser fluence is obtained after measuring the dimensions of the irradiated areas by means of an optical microscopy (or by SEM). After being reflected on the mirror, the beam passes through a filter in order to stop the primary laser wavelength (1064 nm). Then, it is focused perpendicularly on the target surface with an achromatic focusing lens of 100 mm focal length. Samples and their support are handled thanks to an YZ positioning platin, allowing to produce 20 spots at the same sample. For discussion of the ablation effects, comparative investigations are accomplished with a laser spot corresponding to appropriate conditions (fluence and PN) of irradiation.

## 2.3 | X-ray photoelectron spectroscopy

XPS is performed with a Versa probe II ULVAC-PHI in order to identify the elements present in the material before and after ablation. This spectrometer is equipped with the monochromatized source Al  $K\alpha$  ( $h\nu = 1486.6 \text{ eV}$ ). The source is focused on the sample surface, has a diameter of about  $100 \mu\text{m}$  and power of 25 W. All measurements are carried out in an ultra-high vacuum chamber

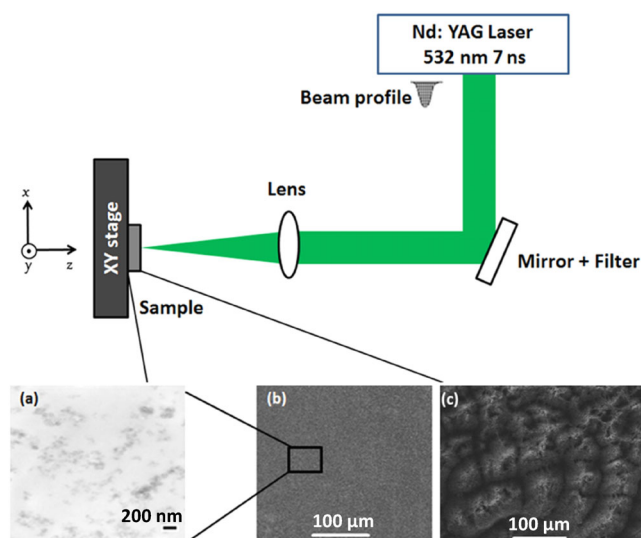


**FIGURE 1** Laser irradiation test setup. (a) micrograph of the composite EBA-20CB obtained by Transmission electron microscopy.<sup>17</sup> (b) and (c) are SEM micrographs of the same composite before and after irradiation at  $215 \text{ mJ/cm}^2$  and 500 pulses, respectively. [Color figure can be viewed at [wileyonlinelibrary.com](http://wileyonlinelibrary.com)]

( $7 \times 10^{-10} \text{ mbar}$ ). The survey spectra are recorded over the 0–1200 eV spectral range, using pass energy set to 23 eV and resolution of 0.5 eV. All XPS spectra binding energies are corrected using the C(1 s) line of  $\text{C}(\text{sp}^2)$  at 284.6 eV. The curve fitting and background subtraction are accomplished using the Casa XPS software. Spectrum curve fitting is performed using Voigt function, convolution product of Gaussian (80%) and Lorentzian (20%) distributions.

## 2.4 | Scanning electron microscopy

SEM analysis of pristine and irradiated surfaces of the samples is performed using a JEOL JSM-6010PLUS/LV SEM. The acceleration voltage is fixed at 5 kV for conducting (8% and 20%) samples and set to 2 kV for sample containing 4% of CB. To probe the nanosized ablation products redeposited at the irradiated surfaces, a ZEISS Gemini SEM 500 70–06 is used. It operates at high vacuum and with short working distance: both parameters increase the resolution and lower the charge-up effect for the nonconductive sample. The acceleration voltage is fixed at 2 kV in all measurements.

## 2.5 | Surface microtopography

Measurement of the irradiated composite AD is carried out using the Microtopographer–Rugotest (STIL CHR

150). This instrument is composed of a white light source (halogen lamp) coupled with a sensor and a spectrometer. The measurement principle is based on confocal microscopy through an extended field chromatic coding. For each irradiated sample, two lateral profiles of the considered surfaces are obtained in (X, Y) directions with information in depth Z by using the XY motorized platform and a suitable optical pencil (OP). The F8 (OP) with measuring range of 0–310  $\mu\text{m}$ , lateral resolution of 2  $\mu\text{m}$ , and working distance of 4.5 mm is used to investigate moderately ablated samples. Another optical pencil F40 with a larger measuring range 0–2650  $\mu\text{m}$ , lateral resolution of 5  $\mu\text{m}$ , and working distance 38 mm is used for larger AD profile examination.

## 2.6 | Thermal conductivity measurement

The thermal diffusivity of non-irradiated samples is measured by laser flash method (NETZSCH LFA447). The square cross section and dimensions are respectively of  $10 \times 10 \times 2$  mm for the EBA/4%CB sample, and  $10 \times 10 \times 1.8$  mm for the EBA/8%-CB and EBA/20%-CB samples. Each sample is analyzed at two different positions and the average value is considered; standard deviation of measured values is less than 5%. The thermal conductivity  $\lambda_{th}$  (W/mK) can be estimated according to  $\lambda_{th} = \chi\rho C_p$ , where  $\rho$  denotes density ( $\text{kg}/\text{m}^3$ ),  $C_p$  (J/kgK) is the specific heat capacity, and  $\chi$  is the thermal diffusivity of the composites ( $\text{m}^2/\text{s}$ ).

## 3 | RESULTS AND DISCUSSION

### 3.1 | Measuring thermal conductivity

The thermal conductivity of EBA/CB composites are listed in Table 1, along with different physical parameters.

These values show that thermal diffusivity and conductivity increase with CB content which is consistent with earlier studies, for example see Reference 19. Furthermore, this trend correlates well with the electric conductivity of our samples, passing from  $10^{-13}$  S/cm for EBA-4CB, to  $10^{-6}$  S/cm for EBA-8CB, and to 0.1S/cm for EBA-20CB.<sup>13,17</sup>

### 3.2 | Probing pulse ablation

Ablation parameters are obtained by measuring the depth of material which is removed from the surface at

each laser pulse. Furthermore, to get a correct estimate of the AD,  $h$ , for our heterogeneous samples, and for the purpose of achieving reproducible etching rate values, it is important to consider the state of dispersion of CB particles within the polymer matrix and their volume fraction. When the fluence is above ablation threshold, it appears that a simple rule of thumb for choosing the specific PN is to consider the etching depth as a multiple of the correlation length, that is, the spatial extent of the largest CB clusters. According to Reference 17, the correlation length for our CB filled polymer samples varies between 1 and 2  $\mu\text{m}$  when CB content is increased from 4% to 12%. For discussion of the ablation effects, comparative investigations of CB filled samples are accomplished with AD per pulse,  $x = h/\text{PN}$ , where PN varies from 1 to 500.<sup>20</sup>

Figure 2 shows  $h$  as a function of PN for different values of laser fluence.

For both composites EBA-4CB and EBA-8CB, the AD increases linearly with PN from 1 to 100 whatever the applied fluence. Beyond this limit, a saturation of the AD is observed with the exception of the highest applied fluence ( $F = 1000$  or  $1050$   $\text{mJ}/\text{cm}^2$  for EBA-4CB and EBA-8CB, respectively) where the AD increases linearly from 1 to 500 pulses. EBA-20CB shows a slight difference in the effect of PN on AD, precisely at the minimum and high values of applied fluences. In fact, saturation in AD is observed from 50 pulses at the minimal fluence 92  $\text{mJ}/\text{cm}^2$ . It is most probably due to the shielding effect of the ablation products formed by accumulating PN and redeposited at the material surface, that is, debris having ablation threshold higher than this applied fluence prevent the laser from hitting the composite material. Furthermore, the ablation rate is increased from 100 to 500 pulses at fluences 474 and  $1.04$   $\text{J}/\text{cm}^2$ . At this elevated PN value and incident laser fluence, it is conceivable that the resulting ablation depth is substantial enough to generate a cavity. Consequently, material removal is facilitated by supplementary factors, including the presence of plasma flow and a shock wave propagating from the bottom of the hole to its entrance. Moreover, these fluence levels lead to attain higher temperatures, predominantly resulting in material sublimation with minimal melting.

Overall, and depending on the applied laser fluence and the volume fraction of CB fillers in the composite, the nanosecond laser processing of these materials can follow three main stages as indicated in Figure 3.

In the first stage, the laser photons excite easily the electrons present in the CB fillers and generate localized heating by absorption of the photon energy. At high CB volume fraction and laser photon energy, the high absorption of laser pulse causes fast heating which could

TABLE 1 Physical properties of the EBA-CB composites and neat EBA at 25°C.

	EBA <sup>18</sup>	EBA-4 CB	EBA-8CB	EBA-20CB
$\rho$ (g/cm <sup>3</sup> )	0.93	0.96	1.00	1.10
$\chi$ (mm <sup>2</sup> /s)	0.1265	0.163 ± 0.003	0.179 ± 0.005	0.364 ± 0.006
$C_p$ (J/gK)	1.693	2.051 ± 0.036	1.713 ± 0.034	1.678 ± 0.017
$\lambda_{th}$ (W/mK)	0.2	0.298 ± 0.005	0.315 ± 0.003	0.726 ± 0.006
$\tau_{RT}$ (ns)	61 × 10 <sup>6</sup>	1982.5	1982.5	55
$L_{th}$ (mm)	7.113 × 10 <sup>-5</sup>	2.553	2.675	3.799
$\alpha_{eff}$ (mm <sup>-1</sup> )	5.7	1.19 × 10 <sup>3</sup>	2.8 × 10 <sup>3</sup>	3.38 × 10 <sup>4</sup>

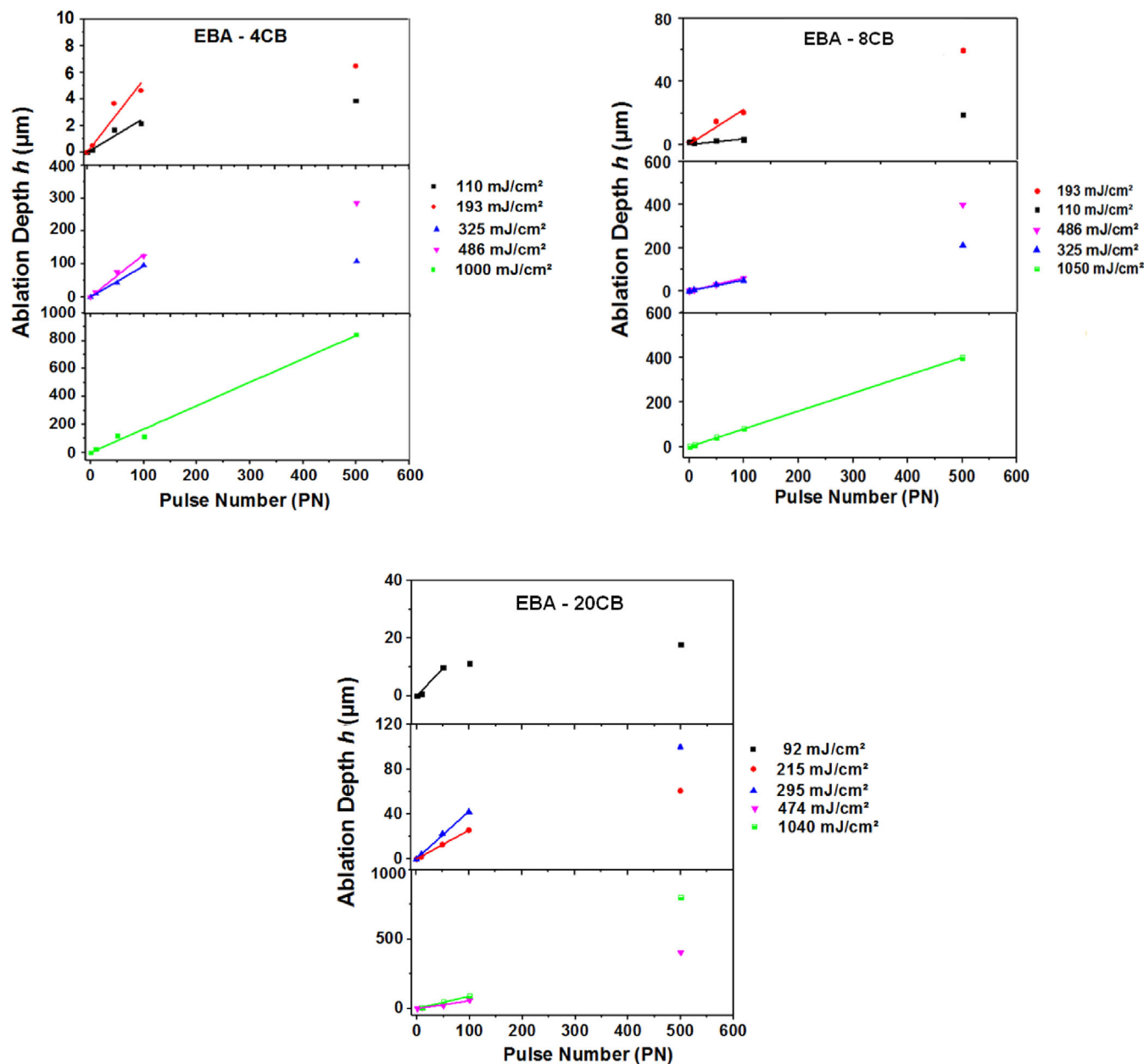


FIGURE 2 Illustrating the effect of PN on the AD  $h$  of EBA-4%, EBA-8%, and EBA-20% samples. Lines present the fits of the linear part of curves. [Color figure can be viewed at [wileyonlinelibrary.com](http://wileyonlinelibrary.com)]

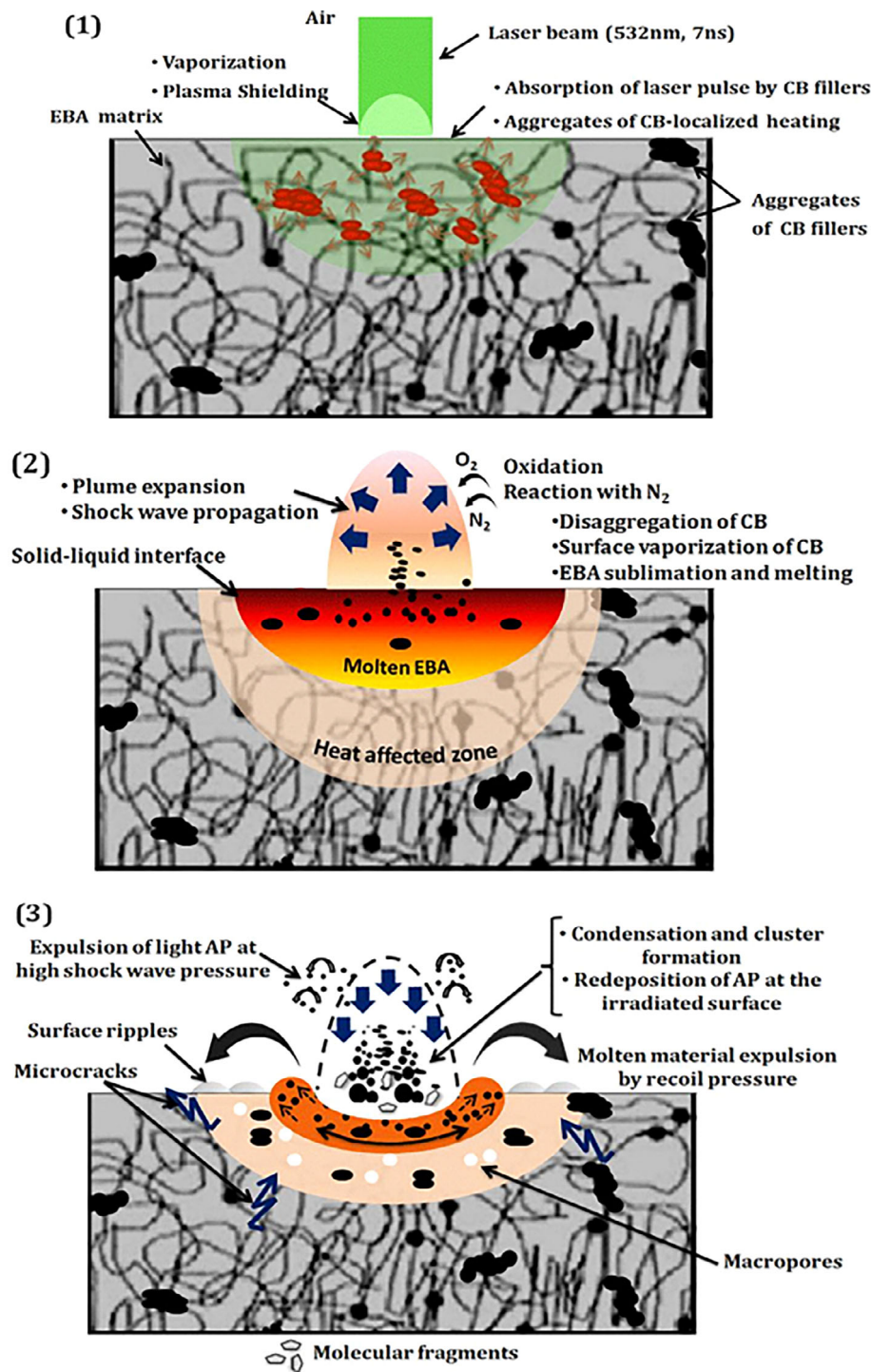
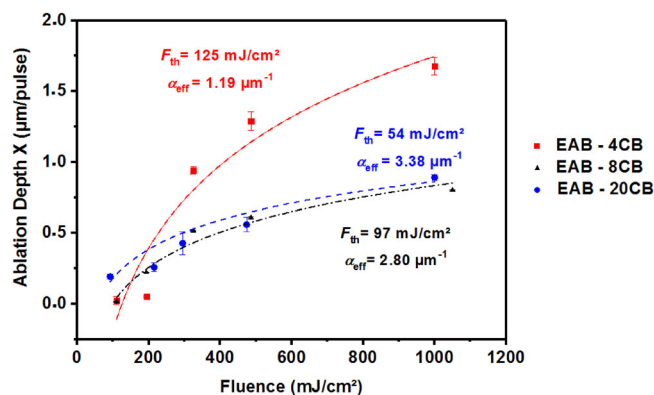


FIGURE 3 Schematic diagram of material removal stages in pulsed-laser ablation of CB-filled polymer in air. (a), (b), and (c) denote the three stage of the nanosecond laser processing of the materials. AP, ablation products. [Color figure can be viewed at [wileyonlinelibrary.com](https://onlinelibrary.wiley.com/doi/10.1002/app.54486)]

be sufficient to cause vaporization of a layer on the CB surface and sublimation of the matrix. Plasma is then generated following gas interaction with the laser pulse and its ionization by releasing electrons. For nanosecond laser pulse, the plasma shielding occurs when the plasma absorbs a fraction of the laser beam via inverse bremsstrahlung. As a result, there is an increase in the temperature and pressure of the plasma due to collisions between atoms, molecules, and ions. Furthermore, the

heating effects induce the melting and subsequent vaporization of the material, as illustrated in the second stage portrayed in Figure 3. After the heating phase, plasma cooling can be impeded through recombination, thermal conduction, and radiative transfer. Reaction between its constituents and the surrounding air-oxygen and nitrogen could lead to deceleration or acceleration of the cooling process for exothermic (combustion) and endothermic reactions, respectively.<sup>21</sup> A part of thermal



**FIGURE 4** AD per pulse,  $x$ , as a function of laser fluence for EBA-4CB, EBA-8CB, and EBA-20CB samples. The dashed lines are fits using Beer Lambert's law. The numbers indicate the ablation thresholds  $F_{th}$  ( $\text{mJ}/\text{cm}^2$ ) and effective absorption coefficient  $\alpha_{eff}$  ( $\mu\text{m}^{-1}$ ). [Color figure can be viewed at [wileyonlinelibrary.com](http://wileyonlinelibrary.com)]

energy in the plasma is converted into kinetic energy leading to the expansion of the gaseous ablation products (ablation plume) into the ambient air. The shock between the ejected molecules and the ambient gas results in the formation of a shock wave. Conversely, while the ablated surface released an intermittently strong shock wave, it also formed a rarefaction wave converging toward the ablation center<sup>3,22</sup> as depicted in the third stage of Figure 3. The last phenomenon causes the re-deposition of the slow particulate ablation products on the substrate (molecules fragments of the matrix) where condensation occurs, while the fate of most of the lightest ablation products depends on the gas flow outside the irradiated substrate.<sup>23</sup> Upon interaction with the material, the laser-induced shock wave undergoes inward propagation as a stress wave consisting of three distinct types of elastic waves: surface wave, longitudinal wave (compression/tension wave), and transverse wave (shear wave). The longitudinal wave is the fastest and the main wave. These waves could induce a strong impact leading to the micro-cracks, or elastic impact, and elastic-plastic impact, ripples formation, and the expulsion of the molten material.<sup>22</sup>

To systematically investigate ablation kinetic and ablation threshold behaviors as a function of CB content, Figure 4 shows a comparison of the AD per pulse. It corresponds to the slope of the linear part of graph presented in Figure 2.

There have been very few attempts to address the question of laser ablation of polymer composites and a limited number of measurements of their etching rate is available.<sup>24</sup> In the context of polymers, and for a limited range of fluence above threshold, it has been suggested that the AD can be estimated by Beer Lambert's law,

$x = \frac{1}{\alpha_{eff}} \ln\left(\frac{F}{F_{th}}\right)$ .<sup>20</sup> Here,  $\alpha_{eff}$  is an effective absorption coefficient determined from a fit to the experimental etching rate versus fluence  $F$  (solid line in Figure 3), and  $F_{th}$  is the threshold fluence which describes the minimum energy which is needed to ablate material. By fitting  $x(F)$  graphs using Beer Lambert's law, the achieved ablation thresholds for samples EBA-4CB, EBA-8CB, and EBA-20CB are respectively 125, 97, and 54  $\text{mJ}/\text{cm}^2$ . Together, these data indicate that the larger CB content in the EBA matrix, the larger effective absorption coefficient, and the smaller ablation threshold.

Upon analyzing the ablation kinetics of the composites, it is evident that the EBA-4CB sample displays the largest AD per pulse, in contrast to the EBA-8CB and EBA-20CB samples, which exhibit similar values (refer to Figure 3). This discrepancy in ablation efficiency suggests that the mechanisms responsible for their ablation are dissimilar. The EBA-4CB composite can be considered as a low-absorbing material at the 532 nm laser wavelength according to its low effective absorption coefficient. In this situation, the possible nanosecond-LA mechanism involved could be addressed mainly by bulk photothermal ablation effect.<sup>25,26</sup> The Photochemical effect which involves a direct chemical bond breaking in composite resulting could be excluded as the energy of the laser photon (2.33 eV) is much less than the bond energies of the EBA-CB composites (ranging from 3.6 to 11.2 eV<sup>27</sup>).

The photothermal effect is a heat transfer problem where carbon particles absorb laser energy and heat the matrix environment.<sup>12</sup> Table 1 shows the calculated heat relaxation time  $\tau_{RT} = \frac{1}{4\alpha_{eff}^2\chi}$  of each composite. Accordingly, the pulse duration is shorter than the time needed for thermal relaxation and diffusion for neat EBA and CB filled EBA samples. This thermal confinement can lead to overheating of the samples beyond boiling temperature or surface evaporation. In addition, the AD of the samples could be correlated with their heat penetration depth  $L_{th} = 2\sqrt{\chi\tau_p}$ .<sup>26</sup> The  $L_{th}$  values are calculated and summarized in Table 1. The larger  $L_{th}$ , the larger the heat affected zone which can result in a slower AD since all irradiated samples have close melting temperatures (90.4–91.5°C).<sup>17</sup> The heated volume in EBA-4CB is rather smaller because of its low thermal conductivity, which helps to focus a high laser energy density in a smaller volume and enhancing the ablation efficiency.

Figure 7 also shows that the ablation rate becomes constant at high fluence ( $> 1000 \text{ mJ}/\text{cm}^2$ ) for all samples. This could be explained by the shielding effect of the plasma-plume as it was reported for most laser ablation of polymers.<sup>3,28</sup> Indeed, at this specific fluence, it is expected that the sublimation of the composites will be fast and exhibit increased efficiency, ultimately resulting



in the formation of plasma within the duration of the laser pulse.

In summary, the photothermal effect is the main mechanism involved in the ablation of the three composites. The EBA-4CB composite has a higher degree of thermal confinement due to its low thermal conductivity, which may explain its high ablation rate.

### 3.3 | Analyzing sample surface by XPS

The EBA-CB samples show diversity in their XPS spectra and are commented below. The details of the spectra of the pristine and irradiated composites at different fluences and PN are relegated to Data S1.

#### 3.3.1 | EBA-20CB

Figure S2 shows the C1s curves of pristine and irradiated EBA-20CB. These graphs indicate the presence of different chemical carbon states because of the asymmetry in the C1s line shape at high binding energy. They exhibit main peaks of  $sp^2$  and  $sp^3$  carbon hybridization at 284.6 eV (C—C/C—H) and smaller peaks associated to amorphous carbon between 285 and 287 eV. The latter can be a signature of a C—O—C/COH, or C—N bonding configurations. The features at energy above 287 eV are characteristics of COO attached to carbon atoms through C  $sp^3$  bonds.<sup>28</sup> The high resolution of O1s spectra are shown in Figure S3. All irradiated samples exhibit two peaks that are overlapping: one at 532 eV and another at 533 eV corresponding to C—O and oxygen-silicon Si—O bonding, respectively.<sup>29</sup> The Si2p peak is observed between 102 and 103 eV in all samples (Figure S4). The presence of silicone in form of silica component can be ascribed to the silane coupling agent which is widely used in rubber technology because it enhances the filler-rubber interaction and improves dispersion. The second origin of silicon elements can be the addition of silica nanoparticles as a co-filler to CB particles in the processing step of samples. Such binary fillers offer a combined advantage such as low hysteresis, good abrasion resistance, and reinforcement.<sup>30</sup> The N1s asymmetric peaks centered at 401 eV is well observed (Figure S5) for irradiated composites at different fluencies and PN.<sup>31</sup> Their deconvolution indicates the presence of three peaks: (1) 398.2 eV for pyridine-like nitrogen ( $C_5H_5N$ ), (2) 400 eV for aromatic amines or pyrrolic nitrogen, and (3) 401.2 eV for quaternary nitrogen (most probably protonated pyridinic N).<sup>32</sup> These species are produced from reaction between the environment air nitrogen  $N_2$  and the ablation gaseous products. According to peak fitting area, the ratios of carbon, oxygen, nitrogen,

and silicon in the above-cited chemical state are calculated for irradiated EBA-20CB. The evolution of these ratios with laser fluence and PN is shown in Figure 5.

Surface analysis before and after irradiation indicates prominent differences. In Figure 5a is observable that the carbon percentage reduces significantly following irradiation, reaching its lowest level (86%) with the lowest fluence (92 mJ/cm<sup>2</sup>) and one pulse. Furthermore, by increasing fluence to 1.04 J/cm<sup>2</sup> while maintaining 1 pulse, the atomic percentage of carbon increases. Likewise, the same trend arises if the PN changes from 1 to 500 at a constant fluence. By the fact, the maximum applied fluence and PN yield slightly higher %C than pristine composite (maximum: 93.8%).

The evolution of the oxygen atomic ratio in the irradiated sample shows the opposite behavior. Figure 5b demonstrates that the fraction of this element increases significantly following irradiation except at 1.04 mJ/cm<sup>2</sup> and 500 PN. At 92 mJ/cm<sup>2</sup> and 1 pulse, the maximum value 8% is obtained. This value decreases constantly with fluence if the applied PN are 1, 100, or 500. A different behavior is observed at 10 and 50 pulses where the percentage of oxygen does not change and fluctuates respectively with fluence. Collectively, these results demonstrate that the sample surface oxidizes under these irradiation conditions and that the larger the level of oxygen reached the smaller the atomic ratio of carbon. The atomic oxygen ratio evolution with fluence as PN is changed can be due to confluence of oxidation of the sample surface and photothermal breakdown of the sample releasing gaseous molecules such as CO and CO<sub>2</sub>. Decomposition into these gaseous products increases the carbon ratio at the surface and it is particularly enhanced by increasing the PN and applying the highest fluence set to 1.04 J/cm<sup>2</sup>.

The evolution of atomic percentage of N1S is shown in Figure 5c. Accordingly, it is difficult to find correlation between the percentage of N1S and fluence or PN. We suggest that the high fluctuation of %N1S is due to the formation and degradation of products containing this element simultaneously by applying a large PN or a high fluence. Deconvolution of the N1S results are presented in Figure A1a–c and discussed in details in Appendix A.

Regarding the atomic ratio of silicon, Figure 5d shows in most cases a decrease with fluence and PN and a slight increase at irradiation conditions: 210 mJ/cm<sup>2</sup>, 1 pulse. This trend is strongly tied to the atomic ratio evolution of carbon.

Now, as concerns the evolution of the chemical state of carbon, the results of C1s deconvolution shown in Figure 6a,b demonstrate that the  $sp^2$  and  $sp^3$  carbon hybridization ratio decreases drastically after ablation of EBA-20CB (from 88.8% to 35% as minima).

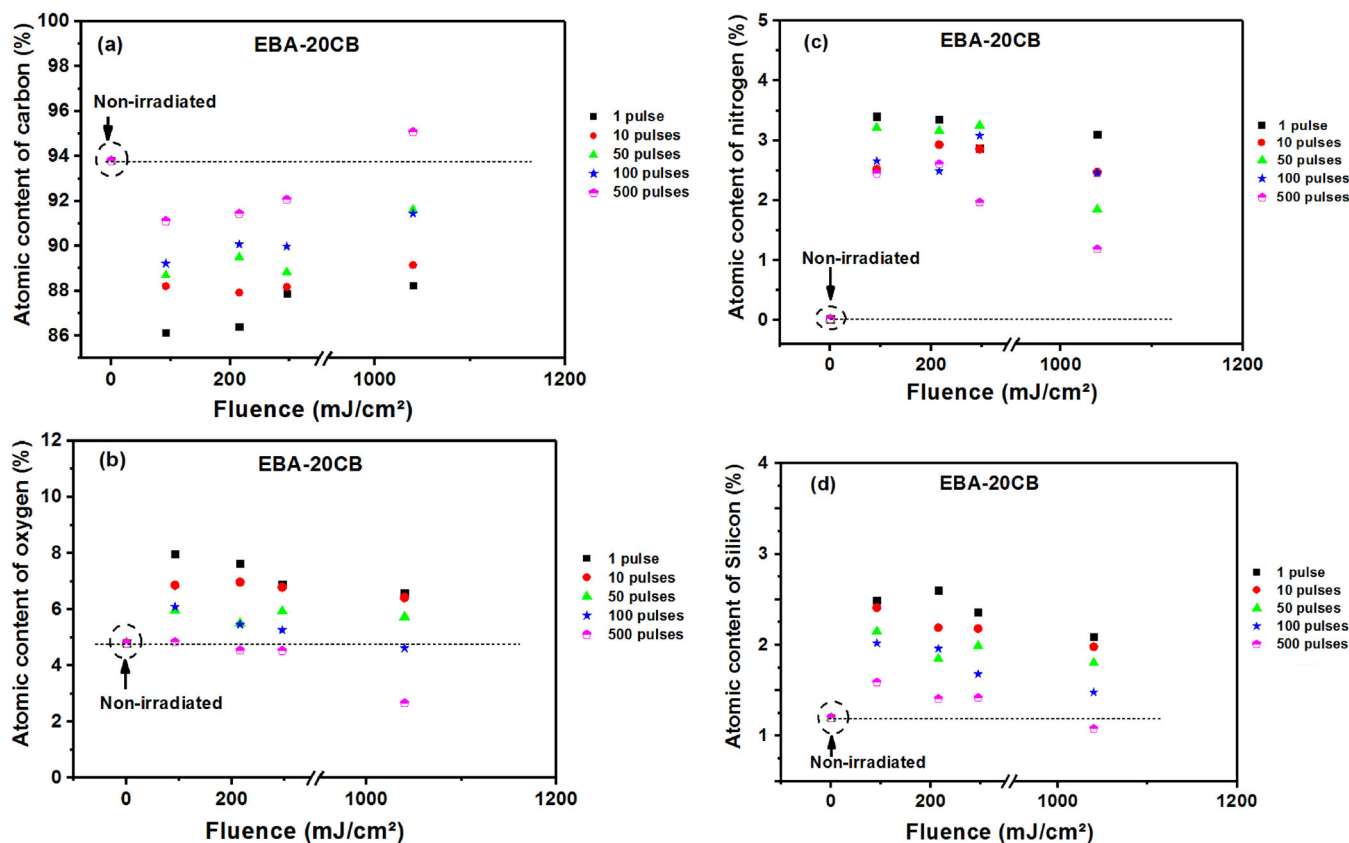


**FIGURE 5** Illustrating the effect of laser fluence and PN on the XPS element analysis of irradiated composite EBA-20CB. (a) %C1s, (b) %O1s, (c) %N1s, (d) %Si2p. Dashed line indicates the atomic percentage of the element in the non-irradiated sample. [Color figure can be viewed at [wileyonlinelibrary.com](http://wileyonlinelibrary.com)]

At 1 pulse, the % of C(sp<sup>2</sup>/sp<sup>3</sup>) increases slightly and almost monotonously with fluence due to thermal ablation of the composite. The last phenomenon is expected to release carbon vapors that condensate partially at the irradiated surface. It appears that degree of carbonization rises in direct proportion to fluence by applying 1 pulse. Furthermore, the amount of this chemical state of carbon decreases slightly from 92 to 210 mJ/cm<sup>2</sup> and increases at higher fluence for PN 10, 50, 100, and 500. Figure 6b shows the evolution of the amorphous carbon (AmC) atomic ratio with fluence and PN. It contrasts with the sp<sup>2</sup>/sp<sup>3</sup> carbon hybridization ratio. The rise in the percentage of amorphous carbon (AmC) is due to the oxidation as well as to the interaction between the carbon vapor generated from sublimation of the composite and the nitrogen in the air. The oxidation results in the development of the COOH/R chemical state of carbon under the irradiation parameters. Figure 6b illustrates that the atomic ratio of COOH/R increases after irradiation, particularly at 92 mJ/cm<sup>2</sup> and with an increase in PN at this fluence. However, when PN is kept constant, the atomic ratio of COOH/R generally decreases with increasing fluence, which correlates with the increase

of the sp<sup>2</sup>/sp<sup>3</sup> hybridized carbon percentage above 210 mJ/cm<sup>2</sup>.

The XPS spectra of pristine and irradiated composites EBA-8CB and EBA-4CB are shown in Figures S6 and S11, respectively. The deconvolution of the C1s curves (Figures S2-8 and S2-12) indicates the presence of the same chemical carbon states found in EBA-20CB. Peak fitting area enables to determine the ratio of elements (carbon, oxygen, nitrogen, and silicon) at 1 and 500 pulses and two laser fluences: (i) 110 mJ/cm<sup>2</sup>, (ii) 192 mJ/cm<sup>2</sup> for EBA-8CB and 325 mJ/cm<sup>2</sup> for EBA-4CB. The evolution of the surface atomic composition with these irradiation conditions is displayed in Figures 7a and 8a.

### 3.3.2 | EBA-8CB

As depicted in Figure 7a,b, the atomic ratio of carbon (C1s) increases by increasing fluence from 110 to 193 mJ/cm<sup>2</sup> at 1 PN or by raising the PN from 1 to 500 at each fluence. All obtained values exceed that of pristine composite. The results also demonstrate a reduction in the percentage of O1s atoms after irradiation, with a

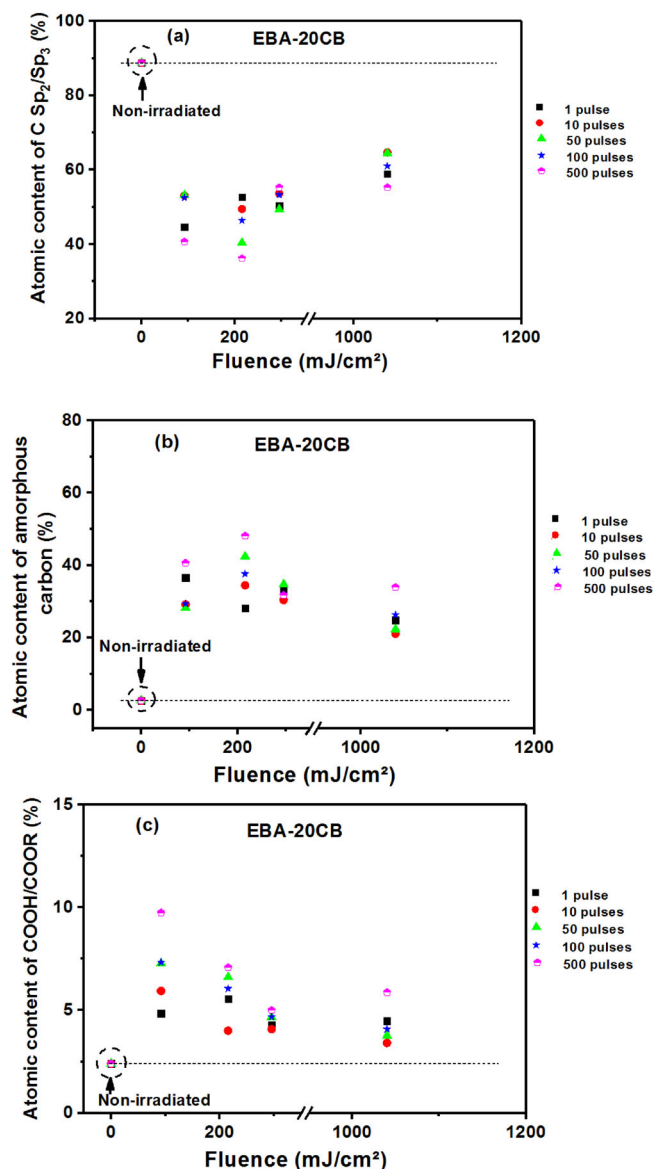


**FIGURE 6** Illustrating the effect of laser fluence and PN on the chemical carbon state ratio after deconvolution of C1S XPS spectra of irradiated EBA-20CB. (a) % C(sp<sup>2</sup>/sp<sup>3</sup>), (b) % amorphous carbon, (c) % COOH/COOR. Dashed line indicates the atomic percentage of these chemical states in the non-irradiated sample. [Color figure can be viewed at [wileyonlinelibrary.com](https://onlinelibrary.wiley.com)]

decrease as fluence is increased at 1 PN, and a different tendency observed when PN is raised to 500 (decrease at 110 mJ/cm<sup>2</sup> and increase at 193 mJ/cm<sup>2</sup>). Upon deconvolution of the C1S peak, the results suggest that the changes in the evolution of amorphous carbon are similar to those observed for C1S with respect to both fluence and PN (↑), while the trend observed for COO is the opposite. Furthermore, the atomic percentage of sp<sup>2</sup>/sp<sup>3</sup> hybridization carbon increases after irradiation and with fluence at 1 PN but decreases if the PN is raised to 500.

According to these results, it appears that when the composite is subjected to laser irradiation at 1 PN, it triggers thermal decomposition, causing a decrease in the percentage of the oxygen and resulting in a carbon-rich surface that is likely to undergo minor oxidation and lead to an increase in AmC and COOH/R percentages. These changes are amplified at greater fluences, causing an increase in the percentage of C1S in the form of AmC and a decrease in the percentage of O1s and COOH/R. Increasing fluence at 1 PN or PN from 1 to 500 leads to a decrease in the atomic ratio of the COO group due to its unstable nature. The COO group decomposes into C-O, which has a lower decomposition temperature (400 K for COO and 1000 K for CO), leading to an increase in the AmC ratio.<sup>33</sup> The observed increase in %O1s with PN at 193 mJ/cm<sup>2</sup> is an exception that can be attributed to significant oxidation of the composite surface. Under these irradiation conditions, the surface becomes enriched in carbon following ablation of the matrix, more reactive with oxygen in the air, and more resistant to ablation (ablation depth saturation at 500 PN: Figure 2).

The N1s peaks of irradiated EBA-8CB composite exhibits as well the formation of NP, NAA and NQ (Figure S10). The largest atomic percentage is reached at the higher PN, that is, 500 at 110 mJ/cm<sup>2</sup> contributing to the increase of AmC%. The atomic ratio of Si2p is reduced after irradiation of EBA-4CB and EBA-8CB samples due to inclusion of nitrogen in their surface structures (Figures S9 and S13).

### 3.3.3 | EBA-4CB

According to Figure 8a, the proportion of carbon atoms increases after exposure to radiation. Additionally, this occurs when the radiation fluence increases from 110 to 325 mJ/cm<sup>2</sup> at 1 PN or at 110 mJ/cm<sup>2</sup> from 1 to 500 PN. At 325 mJ/cm<sup>2</sup>, there is a minor decline in atomic %C as PN increases; nonetheless, the figure remains greater than that of the reference composite. At the same time, the atomic percentage of oxygen develops in an opposite manner to that of carbon. Figure 8b of another section shows that there is a significant decrease in the of sp<sup>2</sup> and sp<sup>3</sup> hybridization carbon ratio due to the increase of the two carbon chemical states ratio, COOH/R and AmC, as a result of irradiation. This is a proof of a minor oxidation of the composite surface while the matrix EBA primarily undergoes sublimation resulting in a decrease of the total oxygen level. Furthermore, at a PN of 1, increasing the fluence to 325 mJ/cm<sup>2</sup> maximizes the % of AmC to 36.56% and produces lower % of COOH/R. However, given that the total oxygen level decreased and that of carbon increased after irradiation,

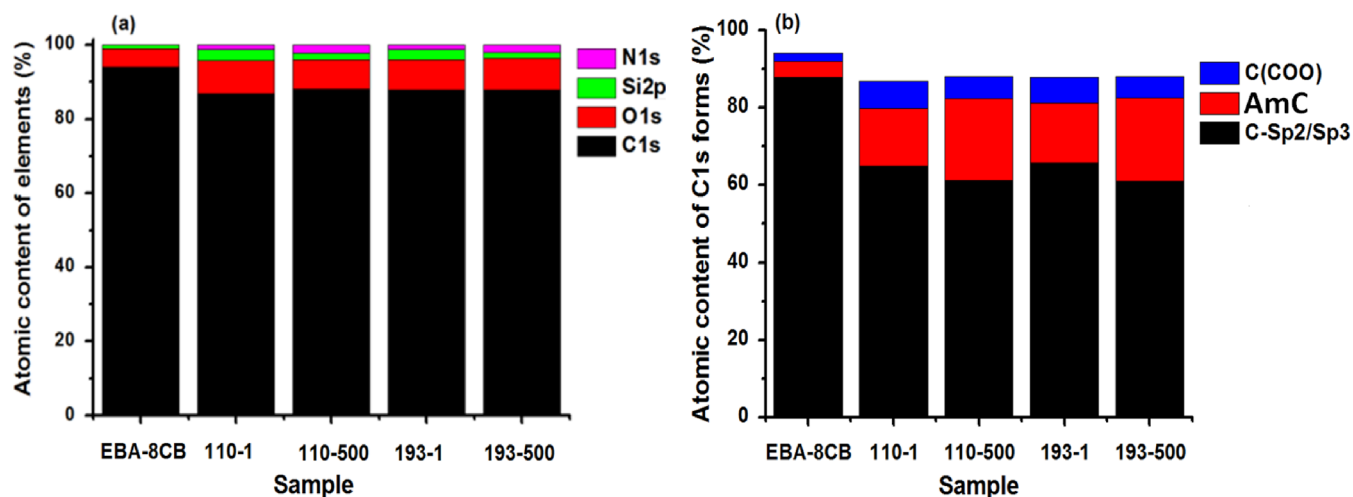


FIGURE 7 (a) Illustrating the surface atomic composition of pristine and irradiated EBA-8CB sample. (b) Atomic composition of different forms of carbon obtained by C1s deconvolution. [Color figure can be viewed at [wileyonlinelibrary.com](https://onlinelibrary.wiley.com/doi/10.1002/app.54486)]

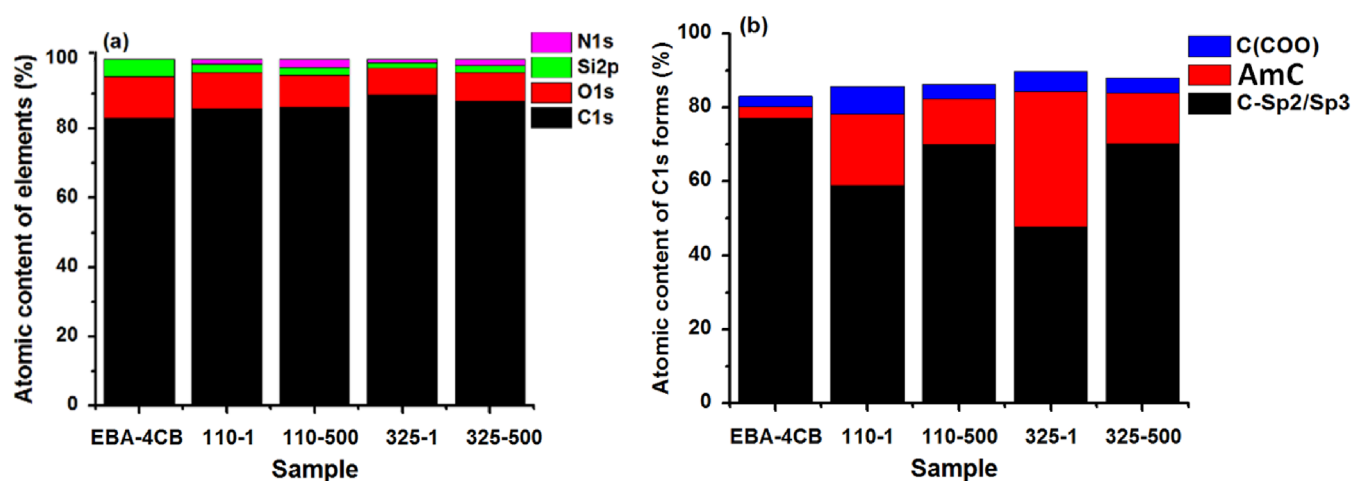


FIGURE 8 Same as in Figure 7 for EBA-4CB sample. [Color figure can be viewed at [wileyonlinelibrary.com](https://onlinelibrary.wiley.com/doi/10.1002/app.54486)]

it is worth noting that the insulating property of EBA-4CB may cause a charge effect, which could widen the C1s peaks and lead to an overestimation of the percentage of AmC at these irradiation conditions.

Besides, the findings suggest that as the PN increases for each fluence, there is a decrease in the proportion of both carbon chemical states and a rise in the sp<sup>2</sup>/sp<sup>3</sup> hybridization carbon ratio, which is contrary to what is observed in EBA-8CB. The dissociation of both AmC and COOH/COOR could be explained by the higher temperatures achieved with the EBA-4CB, which has lower thermal conductivity. As for EBA-20CB, the N1s peaks of irradiated EBA-4CB composite indicates the formation of the three compounds NP, NAA, and NQ contributing to increasing the amorphous carbon form (Figure S5). Likewise, the development of the atomic ratio of silicon with PN or fluence is closely linked to the evolution of the atomic ratio of carbon.

Because the EBA matrix in the composites is produced through high-pressure radical polymerization using double bond-containing monomers, this makes it a good candidate for depolymerization upon laser irradiation by vaporization.<sup>34</sup> In another study, it was reported that the repeated laser pulsing breaks the side chains of EBA monomers, releasing products such as CO<sub>2</sub>, CO, and R—COH due to thermal effects as observed in ester-bond containing polymers (PMMA, PET, and PC).<sup>26</sup> Consequently, it is reasonable to conclude that the rise in oxygen, CO, and COO levels in irradiated EBA-20CB is not a result of EBA oxidation, and this applies similarly to EBA-4CB and EBA-8CB. Moreover, since a more pronounced extent of oxidation is observed in EBA-20CB, it suggests that the CB particle aggregates undergo oxidation when exposed to air during irradiation. Indeed, many studies dealing with laser ablation of low-

Atomic ratio	PN/composite	EBA-4CB	EBA-8CB	EBA-20CB
$C/C_{Ref}$	1	1.03	1.00	0.92
	500	1.04	1.02	0.97
$O/O_{Ref}$	1	0.87	0.98	1.66
	500	0.77	0.87	1.01
$AmC/AmC_{Ref}$	1	6.1	5.6	14.1
	500	3.9	7.9	15.6
$COO/COO_{Ref}$	1	2.6	2.5	2.0
	500	1.3	2.1	4.1

TABLE 2 XPS atomic concentration for pristine and irradiated EBA-CB samples (EBA-4CB and EBA-8CB at 110 mJ/cm<sup>2</sup>, EBA-20CB at 92 mJ/cm<sup>2</sup>).

Note: The reference corresponds to the non-irradiated composite.

dimension graphitic carbon particles in air have proved carbon volatilization at their surface by sublimation and photo-desorption mechanisms (C2 and C3) and their oxidation<sup>35</sup> even at low applied fluence. For example, laser irradiation of Graphene oxide foils with 7 μm in thickness,<sup>36</sup> multi-walled carbon nanotubes (CNT),<sup>37</sup> and soot aggregates produced from ethylene combustion<sup>35</sup> at 532 or 1064 nm have induces an increase in atomic % of the epoxy COC and carboxyl COO groups at their surfaces. The higher applied laser fluence, the more decomposed graphite resulting in amorphous carbon having different structures.<sup>37</sup>

Table 2 provides a comparison between composites on the basis of the chemical composition ratio before and after ablation. In order to achieve this objective, EBA-4CB and EBA-8CB were subjected to radiation of 110 mJ/cm<sup>2</sup> with 1 and 500 pulses whereas EBA-20CB was exposed to the radiation level 92 mJ/cm<sup>2</sup> at the same PNs. Based on these results, it can be inferred that the higher content of CB in the initial sample EBA-20CB promotes the generation of amorphous carbon, primarily through oxidation and secondarily through reaction with nitrogen in the air. Even composite with a low volume fraction of CB fillers (EBA-8CB and EBA-4CB) undergo oxidation according to the increase of AmC and COO ratios.

### 3.4 | Characterizing the structures by SEM imaging

SEM imaging further contributes to provide information of sample surfaces. Here, representative SEM images are commented for each EAB-CB sample.

#### 3.4.1 | EBA-4CB

SEM micrographs in Figures S15, S16, and S17 show the evolution of the EBA-4CB surface microstructure after

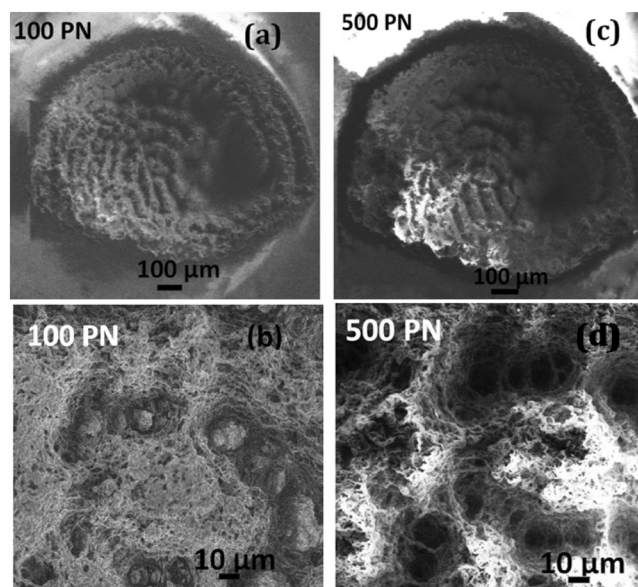


FIGURE 9 SEM micrographs of EBA-4CB irradiated at fluence set to 325 mJ/cm<sup>2</sup> at 100 (a, b) and (c, d) 500 PN.

irradiation with the increase of fluence and PN. The micrographs show that the EBA-4CB undergoes thermal degradation, the development of a porous-like structure due to production of gaseous products, macrocracks, microsized solid fragments, and clusters of nanoparticles. Furthermore, at 193 mJ/cm<sup>2</sup> a dome like structure with a typical size of 16–20 μm is formed and more developed at 325 mJ/cm<sup>2</sup> and 500 PN which is consistent with earlier studies.<sup>9,10,12</sup> At this specific fluence and PN, it appears that the irradiated surface is densely covered with accumulated ablation products since the first applied pulse which aggregates at higher PN as shown in Figure 9. According to XPS results, these products are carbon-rich due to their highest ratio of sp<sup>2</sup>/sp<sup>3</sup> carbon hybridization. Their ablation threshold is higher than this applied fluence. Furthermore, applying higher fluence promotes further vaporization and atomization

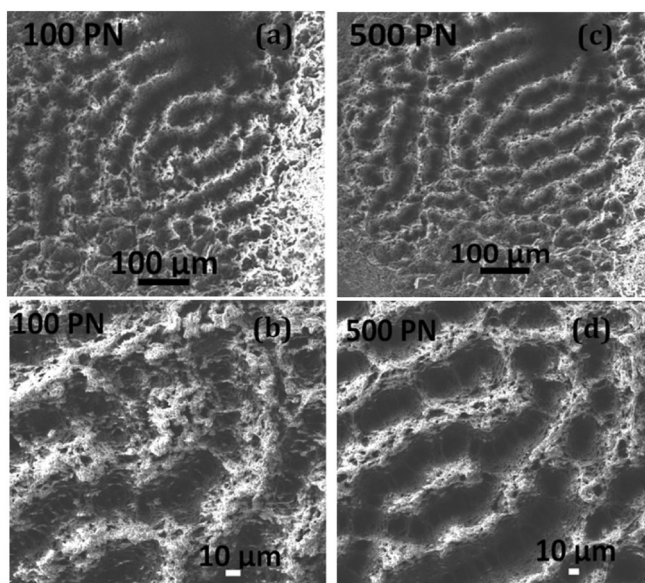


FIGURE 10 SEM micrographs of EBA-8CB irradiated at fluence set to  $193 \text{ mJ/cm}^2$  at 100 (a, b) and (c, d) 500 PN.

of the target resulting probably in the preferential formation of smaller ablation products and a high recoil pressure which enhances ablation efficiency by ejecting ablation products to the periphery of the irradiated surface.<sup>34</sup>

### 3.4.2 | EBA-8CB

Figures S18, S19, and S20 exhibit SEM micrographs of EBA-8CB subjected to irradiation at different fluences and PN. The surface structure of EBA-8CB shares many similarities with that of EBA-4CB. The photothermal effect generates a high density of macropores, macrocracks, melting, and ablation product aggregates both on and beneath the irradiated surface. To create a dome-like structure on the irradiated surface, a large amount of carbon-rich ablation products must accumulate and aggregate on the surface, and the rarefaction of the shock wave must have low pressure as was demonstrated in the case of EBA-4CB. According to Figure 10, these conditions are met when the fluence reaches  $193 \text{ mJ/cm}^2$  for EBA-8CB. Consequently, even though the amount of ablation products is nearly identical for both composites at this fluence, EBA-8CB demonstrates the formation of dome-like structures at a lower fluence. When the fluence is increased to  $295 \text{ mJ/cm}^2$ , the efficiency of ablation improves, resulting in a minor portion of ablation products being redeposited on the irradiated substrate. This can be attributed to the fact that EBA-8CB has a lower ablation threshold, leading to a higher atomization of the target, prompt ionization, and further dissociation of large

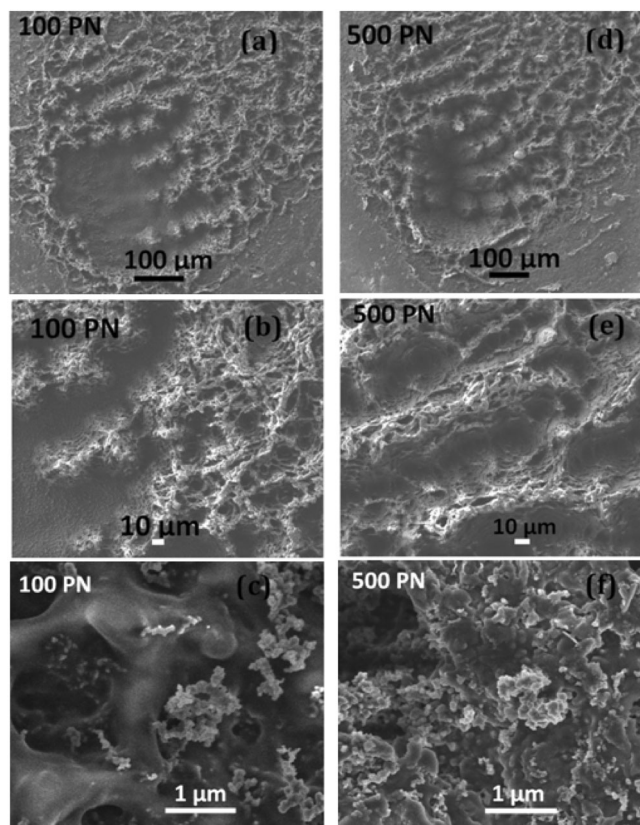


FIGURE 11 SEM micrographs of EBA-20CB irradiated at fluence set to  $92 \text{ mJ/cm}^2$  at 100 (a–c) and 500 PN (d–f). (c) and (f) illustrate aggregates of the ablation products at the apex of the dome-like structure.

clusters in the ablation plume. As a result, there is a higher intensity of lighter species that flow outside the irradiated substrate<sup>38</sup> (see Figure S20).

### 3.4.3 | BA-20CB

Figures S21 to S24 present SEM micrographs of irradiated EBA-20CB. The results indicate that the high absorption coefficient and high thermal diffusion length of EBA-20CB resulted in an extended thermal damage of both the irradiated surface and the underlying material. Furthermore, the material experiences melting and swelling even at laser fluences below its ablation threshold ( $40 \text{ mJ/cm}^2$ , 100 PN). At a fluence of  $92 \text{ mJ/cm}^2$  and 500 PN, the ablation products are mostly interconnected clusters or aggregates of nanoparticles, which are deposited and accumulated at the irradiated surface to form a dome-like structure. Based on XPS results, we suggest that these products are extensively oxidized and contain a significant amount of COOH/COOR groups. Furthermore, EBA-20CB has the lowest specific fluence compared to other composites at which the dome-like structure covers most

of the irradiated surface due to its high CB filler content. This finding is similar to the comparison made between EBA-4CB and EBA-8CB (Figure 11).

## 4 | CONCLUSION

The laser ablation of an elastomer EBA, filled with different concentrations (4%, 8%, and 20%) of CB nanoparticles, was investigated and compared using nanosecond laser pulse. The photothermal effect is considered to be the primary mechanism involved in the laser ablation of these composites. In the case of EBA-4CB, this composite exhibits the highest level of thermal confinement, which enhances its laser ablation efficiency (AD). XPS results confirm that all composite samples undergo oxidation and react with air-nitrogen during irradiation, with the highest degree of oxidation observed in the sample containing 20% of CB. More importantly, the formation of a dome-like microstructure on the composite surface is primarily attributed to the shielding effect resulting from the significant redeposition of ablation debris back onto the surface and the low shock wave pressure induced during plume expansion and cooling.

### AUTHOR CONTRIBUTIONS

**I. El Aboudi:** Conceptualization (equal); investigation (equal); resources (equal); visualization (equal); writing – original draft (equal). **Z. Bouyahia:** Data curation (equal); investigation (equal); software (equal). **D. He:** Data curation (equal); investigation (equal). **J. Bai:** Investigation (equal); writing – review and editing (equal). **A. Mdarhri:** Conceptualization (equal); resources (equal); validation (equal). **C. Brosseau:** Conceptualization (equal); supervision (equal); validation (equal); writing – review and editing (equal). **A. Benayad:** Investigation (equal); software (equal). **F. Charlot:** Investigation (equal); software (equal). **M. Elazhari:** Investigation (equal). **G. Pecastaings:** Investigation (equal); software (equal).

### DATA AVAILABILITY STATEMENT

The data that support the findings of this study are available from the corresponding author upon reasonable request.

### ORCID

C. Brosseau  <https://orcid.org/0000-0002-2629-0267>

### REFERENCES

- [1] M. S. F. Lima, J. M. S. Sakamoto, J. G. A. Simoes, R. Riva, *Phys. Procedia* **2013**, *41*, 572.

- [2] T. Ibatan, M. S. Uddin, M.-A.-K. Chowdhury, *Surf. Coat. Technol.* **2015**, *272*, 102.
- [3] S. R. Kumara, B. Liesa, X. Zhanga, H. Lyub, H. Qina, *Polym. Int.* **2019**, *68*, 1391.
- [4] P. Moreno, C. Mendez, A. Garcia, I. Arias, L. Roso, *Appl. Surf. Sci.* **2006**, *252*, 4110.
- [5] X. Zhang, D.-T.-A. Zeng, A. Matthews, V.-E. Igartua, J. Rodriguez, V. Contreras Fortes, S. de Viteri, F. Pagano, B. Wadman, E. D. Wiklund, E. Van der Heide, *Friction* **2016**, *4*, 89.
- [6] U. Pettersson, S. Jacobson, *Tribol. Int.* **2003**, *36*, 857.
- [7] A. Dunn, K. L. Wlodarczyk, J. V. Carstensen, E. B. Hansen, J. Gabzdyl, P. M. Harrison, J. D. Shephard, D. P. Hand, *Appl. Surf. Sci.* **2015**, *357*, 2313.
- [8] M. Bolle, S. Lazare, *J. Appl. Phys.* **1993**, *73*, 3516.
- [9] J. F. Silvain, H. Niino, S. Ono, S. Nakaoka, A. Yabe, *Appl. Surf. Sci.* **1999**, *141*, 25.
- [10] S. Ono, S. Nakaoka, J. Wang, H. Niino, H. A. Yabe, *Jpn. J. Appl. Phys.* **1997**, *36*, L1387.
- [11] H. Niino, J. Ihlemann, S. Ono, A. Yabe, *J. Photopolym. Sci. Technol.* **2000**, *13*, 167.
- [12] J. F. Silvain, H. Niino, A. Yabe, *Compos. Part A Appl. Sci. Manuf.* **2000**, *31*, 469.
- [13] A. Mdarhri, C. Brosseau, F. Carmona, *J. Appl. Phys.* **2007**, *101*, 084111.
- [14] C. Brosseau, *Surf. Coat. Technol.* **2011**, *206*, 753.
- [15] H. M. Zidan, M. A. Elnader, *Phys. B* **2005**, *355*, 308.
- [16] H. Chang, T. T. Charalampopoulos, *Proc. R. Soc. A.* **1990**, *430*, 577.
- [17] A. Mdarhri. Ph.D. Thesis, University of Bordeaux, France. **2007**.
- [18] G. Wypych, *Handbook of Polymers*, ChemTec Publishing, Toronto **2012**.
- [19] Y. Agari, T. Uno, *J. Appl. Polym. Sci.* **1985**, *30*, 2225.
- [20] P. E. Dyer, *Appl. Phys. A Mater. Sci. Process.* **2003**, *77*, 167.
- [21] J.-L. Gottfried, *Phys. Chem. Chem. Phys.* **2014**, *16*, 21452.
- [22] L. Zhou, W. He, *Gradient Microstructure in Laser Shock Peened Materials-Fundamentals and Applications*, Springer Series in Materials Science, Vol. 314, Springer, China **2021**, p. 16.
- [23] F. R. Wagner, *High Power Laser Matter Interaction: Micro Machining and Laser Induced Damage Using Nanosecond Lasers*, Aix-Marseille University, France **2012**.
- [24] V. Oliveira, S. P. Sharma, M. F. S. F. de Moura, R. D. F. Moreira, R. Vilar, *Opt. Lasers Eng.* **2017**, *94*, 37.
- [25] E. Spyratou, M. Makropoulou, A. A. Serafetinides, *Lasers Med. Sci.* **2008**, *23*, 179.
- [26] L. Urech, T. Lippert, in *Photochemistry and Photophysics of Polymeric Materials* (Ed: N. S. Allen), John Wiley & Sons, Inc., Hoboken, NJ **2010**, p. 541.
- [27] A. Vogel, V. Venugopalan, *Chem. Rev.* **2003**, *103*, 577.
- [28] I. Elaboudi, S. Lazare, C. Belin, D. Talaga, C. Labrugère, *Appl. Phys. A Mater. Sci. Process.* **2008**, *92*, 743.
- [29] R. Aghaei, A. Eshaghi, *J. Alloys Compd.* **2017**, *699*, 112.
- [30] X. Wang, L. Wu, H. Yu, T. Xiao, H. Li, J. Yang, *e-Polymers* **2021**, *21*, 279.
- [31] L. López-Vilanova, E. Espí, I. Martínez, J. L. G. Fierro, T. Corrales, F. Catalina, *Polym. Degrad. Stab.* **2013**, *98*, 2146.
- [32] R. J. J. Jansen, H. Van Bekkum, *Carbon* **1995**, *33*, 1021.
- [33] W. Shen, Z. Li, Y. Liu, *Chem. Eng.* **2008**, *1*, 27.

- [34] T. Lippert, *Polymer* **2005**, *2*, 525.
- [35] H. A. Michelsen, A. V. Tivanski, M. K. Gilles, L. H. van Poppel, M. A. Dansson, P. R. Buseck, *Appl. Opt.* **2007**, *46*, 959.
- [36] L. Torrisia, M. Cutroneo, L. Silipignia, M. Fazioc, A. Torrisi, *Phys. Solid State* **2019**, *61*, 1327.
- [37] P. D. Kichambare, L. C. Chen, C. T. Wang, K. J. Ma, C. T. Wu, K. H. Chen, *Mater. Chem. Phys.* **2001**, *72*, 218.
- [38] L. Zhang, C. Feng, Q. Xiao, R. Hai, H. Ding, *Plasma Sci. Technol.* **2015**, *17*, 958.
- [39] J. R. Fels, F. Kapteijn, J. A. Moulijn, Q. Zhu, K. M. Thomas, *Carbon* **1995**, *33*, 1641.
- [40] I. T. Zimmermann, F. Schüth, *Chem. Rev.* **2014**, *114*, 1761.

## SUPPORTING INFORMATION

Additional supporting information can be found online in the Supporting Information section at the end of this article.

**How to cite this article:** I. El Aboudi, Z. Bouyahia, D. He, J. Bai, A. Mdarhri, C. Brosseau, A. Benayad, F. Charlot, M. Elazhari, G. Pecastaings, *J. Appl. Polym. Sci.* **2023**, *140*(40), e54486. <https://doi.org/10.1002/app.54486>



## APPENDIX A

## A.1 | ANALYSIS OF THE NITROGEN CONTAINING ABLATION PRODUCTS OF EBA-20CB BY X-RAY PHOTOELECTRON SPECTROSCOPY

As mentioned in Section 3.3, three N-containing compounds are identified at the irradiated surface of

EBA-20CB: N-pyridine, N-pyrrolic, or N-aromatic amines and N-quaternary designated by NP, NAA, and NQ, respectively. Figure A1a–c shows that the most abundant product is NAA and it is highly produced at 1 pulse and fluence lower than  $210 \text{ mJ/cm}^2$ . However, it is difficult to find a correlation between the atomic ratio evolution of these containing nitrogen components and the laser irradiation settings. In fact, one

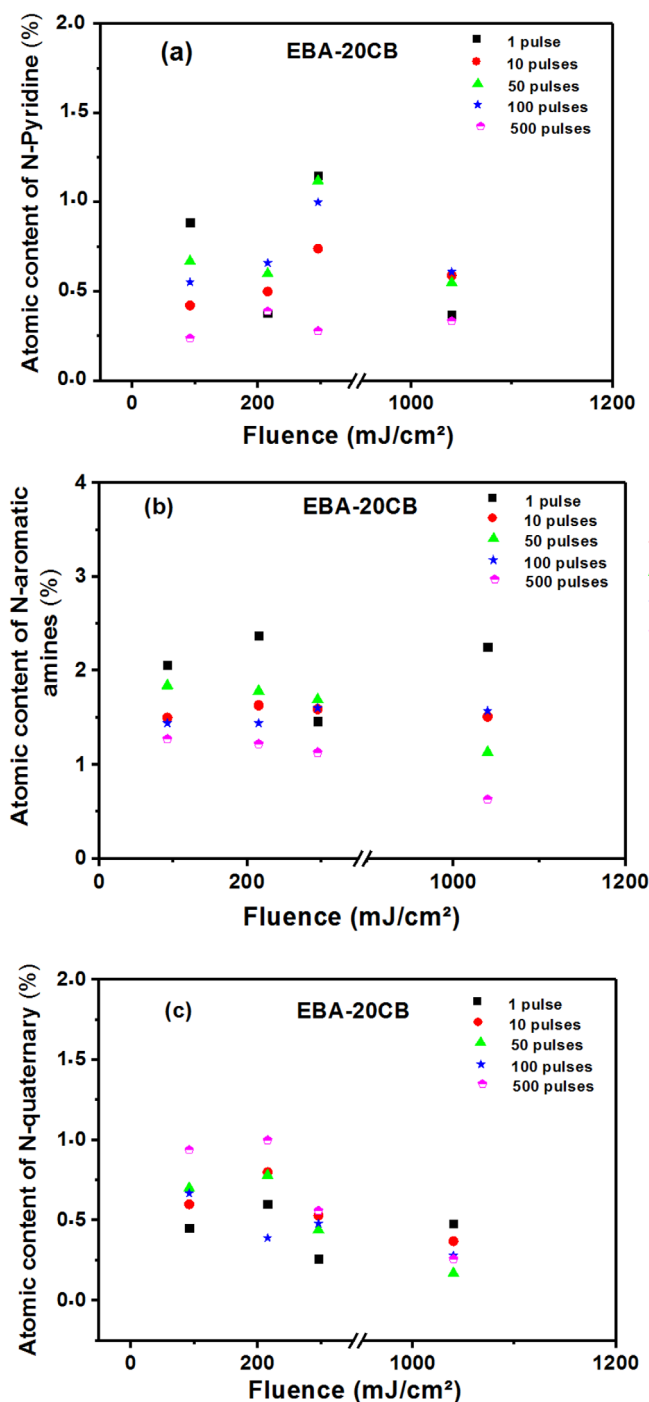


FIGURE A1 Illustrating the effect of laser fluence and PN on the chemical nitrogen state ratio after deconvolution of N1s XPS spectra of irradiated EBA-20CB. (a) % N Pyridinic, (b) % N aromatic amines, (c) % N-quaternary. [Color figure can be viewed at [wileyonlinelibrary.com](http://wileyonlinelibrary.com)]

functional form of nitrogen can be converted into another depending on the laser fluence and the accumulated PN. For example, it is possible that at high fluence or PN, the NAA compounds are converted into NQ and NP. Furthermore, a possible reaction of

cycloaddition between NQ and acetylene vapors resulting from photothermal degradation of EBA in the ablation plume leads to the formation of pyridine molecules. Oxidation of the pyridinic N at high temperature induces conversion of NP to NAA.<sup>39,40</sup>